

Scientific paper

Synthesis and Characterization of Ca and Ba Doped LAMOX Materials and Surface Study by X-ray Photoelectron Spectroscopy

Ammar Khaled,¹ Jean-Jacques Pireaux² and Smail Khelili^{1,*}¹ Département de Chimie, Faculté des Sciences Exactes et SNV, Université de Jijel, BP. 98, Ouled Aissa 18000 Jijel, Algérie² University of Namur, Research Center on Physics of Matter and Radiation (PMR), 61, rue de Bruxelles, 5000 Namur, Belgique* Corresponding author: E-mail: skhelili@yahoo.fr;
Phone: +213 345039114 ; Fax : +213 345039114

Received: 03-02-2012

Abstract

(La_{1-x}Ca_x)₂Mo₂O_{9-δ} and (La_{1-x}Ba_x)₂Mo₂O_{9-δ} (x = 0.05, 0.1, 0.15, 0.2) materials were prepared at 800 °C by co-precipitation method and characterized by X-ray diffraction and scanning electron microscope. The XRD diagrams showed the presence of CaMoO₄ and BaMoO₄ secondary phases only at high contents of the dopants. X-ray photoelectron spectroscopy was used to study the surface chemical structure of doped and undoped materials (La₂Mo₂O₉). It was found that the La and Mo atoms had 3+ and 6+ valence states, respectively. The absence of carbides and carbonates at surface suggests that, the unavoidable carbon contamination did not interact with the metal atoms, which allows applications using carbonaceous fuels, and, that the formation of secondary phases did not influence the surface state. XPS spectra show that the covalent character of the La–O bond was enhanced with calcium doping as compared to barium, predicting interesting conductive and catalytic properties of the materials.

Keywords: Mixed metal oxides, LAMOX, surface characterization, XPS

1. Introduction

The mixed oxides composed of lanthanum and transition metals still attract a great interest because of their interesting physico-chemical properties fundamentally and technologically. The LAMOX group, for which the parent compound is lanthanum molybdate La₂Mo₂O₉, had been the subject of a hundred publications during these last ten years. Indeed, it showed interesting electrochemical properties as a solid electrolyte solution, making it a good candidate for technological applications in solid oxide fuel cells (SOFCs) and oxygen pumps sensors.

Ultrafine powders of LAMOX were prepared by a sol-gel method and used as catalysts in the oxidation of organic compounds.^{1,2} It was found that the decreasing of particle size of La-Mo or Ce-Mo mixed oxides down to the nanometer scale, the remarkably improved the reactivity of oxygen ions and the selective oxidation of toluene to

benzaldehyde. However, studies on lanthanum-molybdenum or cerium-molybdenum mixed oxides as catalysts for selective oxidation improvement or other oxidation reactions are quite limited.

Thereafter, P. Lacorre³ and F. Goutenoire⁴ have proclaimed that La₂Mo₂O₉ prepared by the ceramic method, was a new fast oxygen ions conductor. The compound can exist in two crystalline forms. The monoclinic α La₂Mo₂O₉ or distorted cubic form exists at low temperature but is transformed at 580 °C to the β La₂Mo₂O₉ cubic form. The ionic conductivity of the material is then increased by two orders of magnitude when passing from the α to the β form, for which the maximum conductivity value was recorded at 800 °C. In order to suppress the phase transition and stabilize the β form at low temperature, these authors announced the possibility of doping this material, which is obtained by substituting a fraction of lanthanum ions La³⁺ by K⁺, Sr²⁺, Ba²⁺ or Bi³⁺, while the

molybdenum cation Mo^{6+} can be substituted by V^{5+} , S^{6+} , Cr^{6+} or W^{6+} . This material became a potential candidate to replace yttria-stabilized zirconia (YSZ) solid electrolyte material, which is conventionally used in SOFCs operating at high temperatures (between 800 and 1000 °C).⁵ The elevated operation temperatures of this electrolyte limit the choice of appropriate SOFC components, resulting in the use of expensive materials with relative low lifetime by embrittlement of fuel cell components. Because of this, new families of ionic conductors of different crystal structures including the LAMOX family were studied.^{6–10} At high temperatures, the conductivity of β form is comparable to that doped with other elements, including the alkaline earth elements such as Ca and Ba. The research was then directed towards lowering the operating temperature to the so called intermediate ones (500–600 °C) and to keep the low temperature β form by doping the parent material. Thus, doped materials have a dual influence, on one hand on the improving the transport properties of materials and, on the other hand, they entirely suppress the phase transition. We believe that doping by calcium and barium could respond to this need. There are a few works that dealt with the partial substitution of La sites by alkaline earth cations like Ca^{2+} , Sr^{2+} or Ba^{2+} , to suppress the phase transition, and to improve the ionic conductivity.^{6–10}

For SOFCs operating at high temperatures, the electrochemical oxidation of the fuel (like H_2 , CH_4 , CO , or other hydrocarbons), occurs at the anode-solid electrolyte interface.¹¹ One of the fundamental requirements for an electrolyte or catalyst material is its inertness towards fuels as well as oxidants. Therefore, heat treatment or calcinations in air at high temperature for several hours may be regarded as a stability test of material in an operating environment.

Certainly, the study of the material surface composition is a key analysis in order to provide a vital link to the overall operating behavior of the whole system. It is expected that knowledge of the composition and surface properties of the material can give a better idea on its electrochemical and catalytic properties. However the surface characterization of LAMOXs and their derivatives are not numerous, in particular by X-ray photoelectron spectroscopy (XPS).^{12,13} In this context, by means of XPS, we aim to give a clear picture of the bonds involving the cations and their valence state on the surface of two series of mixed oxides, namely the $(\text{La}_{1-x}\text{Ba}_x)_2\text{Mo}_2\text{O}_{9-8}$ (LBM) and the $(\text{La}_{1-x}\text{Ca}_x)_2\text{Mo}_2\text{O}_{9-8}$ (LCM) materials.

In fact, it is known that the preparation method of the LAMOX oxides directly influences the microstructure of the crystalline powders, with the consequence that large porosity and low connectivity between the grains have a negative effect on the transport properties.¹⁴

In our case, we used the wet co-precipitation method for the samples preparation. This provides homogeneous nano scaled powders.^{1,14–17} We introduced increasing amounts of Ca^{2+} and Ba^{2+} doping agents to substitute the

La^{3+} cation sites. In this report, we study the surface state of LCM and LBM materials, elaborated at 800 °C, by XPS. We also used the thermogravimetric analysis and differential scanning calorimetry (TG-DSC) to study the thermal behavior and X-ray diffraction (XRD) to confirm the presence of the target phases, while the surface morphology of the synthesized materials was analyzed by scanning electron microscopy (SEM).

2. Experimental

2.1. Chemistry

The starting compounds used for the synthesis of the materials were ordered from Sigma-Aldrich: $\text{La}(\text{NO}_3)_3 \cdot 6\text{H}_2\text{O}$ (98%), $\text{Ba}(\text{NO}_3)_2$ (99.5%), $\text{Ca}(\text{NO}_3)_2 \cdot 4\text{H}_2\text{O}$ (98.5%), $(\text{NH}_4)_6\text{Mo}_7\text{O}_{24} \cdot 4\text{H}_2\text{O}$ (99%).

An aqueous solution of $\text{Ba}(\text{NO}_3)_2$ or $\text{Ca}(\text{NO}_3)_2$ was added dropwise in appropriate quantities to an aqueous solution of $\text{La}(\text{NO}_3)_3 \cdot 6\text{H}_2\text{O}$ and magnetically stirred. Then, an aqueous solution of $(\text{NH}_4)_6\text{Mo}_7\text{O}_{24} \cdot 4\text{H}_2\text{O}$ was added dropwise. A white precipitate was formed gradually, showing a final pH of 2. The final mixture was slowly heated in air at 70 °C for 2 to 3 days to evaporate the majority of the solvent. The white substance formed was crushed in a mortar, dried at 120 °C for several hours and then annealed at 500 °C and 800 °C for 6 hours. The dopants quantities introduced were $x = 0.05, 0.1, 0.15$ and 0.2 which correspond to 5, 10, 15 and 20% respectively. We noticed that, one can even use a solution of lanthanum oxide in dilute nitric acid instead of the lanthanum nitrate, and a solution of molybdenum oxide in ammonia can be used instead of the aqueous solution of ammonium molybdate.

2.2. Sample Characterization

Thermal analysis of the powders, dried at 120 °C, was carried out in air by SETARAM TG-DSC 111 analyzer. The X-ray diffraction characterization was carried out at room temperature, with the $\text{Cu}_{K\alpha}$ monochromatic radiation ($\lambda = 0.15418$ nm) of a D8 Advance Bruker NXS diffractometer, operating at the accelerating voltage of 40 kV and filament current of 40 mA. Data were collected between 10° and 80° at 0.04°/step for a counting time of 5s.

Imaging by scanning electron microscope was performed using a Philips (XL 20, 15 keV) model. Due to the insulating character of the samples, metallization has been carried out to prevent the electrical charge accumulation. The powders were spread on a double-sided conductive adhesive and glued on a small metal plate of 1cm².

XPS measurements were performed on a Hewlett-Packard 5950A spectrometer equipped with a monochromatic $\text{Al}_{K\alpha}$ source (1486.6 eV). The energy resolution is optimized for constant pass energy of 150 eV, in any acquisition mode; the resulting nominal full width at half

maximum measured on the Au 4f line is 0.7 eV. The sample was out gassed under vacuum at $\sim 10^{-8}$ torr for several hours (~ 12 h) before the analysis. Charging effects (inducing the shift of peaks) were observed in all measurements and were neutralized using a flood gun typically operated at 2 eV. All the spectra were calibrated in binding energy with reference to the C 1s peak of contamination fixed at 284.6 eV.¹⁸ The standard deviation for the BEs was 0.1 eV. Since all the samples are solids, the Fermi level is used as a reference. The photoemission peaks were fitted with mixed Gaussian–Lorentzian functions using a home-developed least squares curve-fitting program (Winspec). Either linear and or Shirley backgrounds were used depending on the shape of the spectra. The surface atomic composition was calculated by the integration of the peak areas on the basis of the Scofield's sensitivity factors.¹⁹ We also chose the C1s peak of contamination as internal reference to calculate the atomic composition (in at. %) according to equation 1.

$$\frac{[X]}{[C]} = \frac{N_X \cdot \sigma_C \cdot \lambda_C}{N_C \cdot \sigma_X \cdot \lambda_X} \quad (1)$$

Where N is the experimentally determined peak intensity of X and carbon C subshell atoms affected by the photoionization, σ is the sensitive factor and λ is the mean free path of photoelectron in the sample.

As suggested for inorganic solids and binding energies below 1100 eV, we took $\lambda_{x,k} = E_C^{0.75}$ where E_C is the kinetic energy of electron ejected from the k^{th} shell of an atom at the surface.

3. Results and Discussion

3.1. Thermal Analysis

Figure 1 presents the thermal behavior of the two samples LCM and LBM with high dopant contents ($x = 0.2$). The heat flow (or, differential scanning calorimetry, DSC) curve is accompanied with the thermogravimetry (TG) one, to know the nature of thermal behavior of the samples. The curves of the two systems have almost the same form; there are series of decomposition steps with successive inflexion points indicated on the derivative thermogravimetry (DTG) curves. Regarding the LCM system, the TG signal indicates that the mass losses appear at 100, 268, 302 and 409 °C (67, 140, 263, 311, 414 °C for LBM system) as well as a little change at about 163 °C (512 and 555 °C for LBM system). Above 409 °C, the curve presents a plateau indicating the formation of pure phase (Above 555 °C for LBM system). The total mass loss for the two samples is almost the same ($\sim 41\%$ for LCM and $\sim 42\%$ for LBM).

In the two cases, endothermic peaks below 200 °C characterize the evaporation of residual water. The thermal decomposition of nitrates with high mass loss occurs

at 268 °C and 302 °C for the LCM system and at 263 °C and 311 °C for the LBM system respectively. Peaks, at 410 °C for LCM system and 415 °C for LBM system, could be attributed to the elimination of decomposed materials. The two small endothermic peaks at 512 °C and 555 °C for LBM system can be attributed to the decomposition of impurities. From the results of thermal analysis, we can say that, the thermal decomposition of LCM 0.2 sample is even below 500 °C and for LBM 0.2 is almost 600 °C. In our study, the samples were annealed at 800 °C to have well crystallized materials.

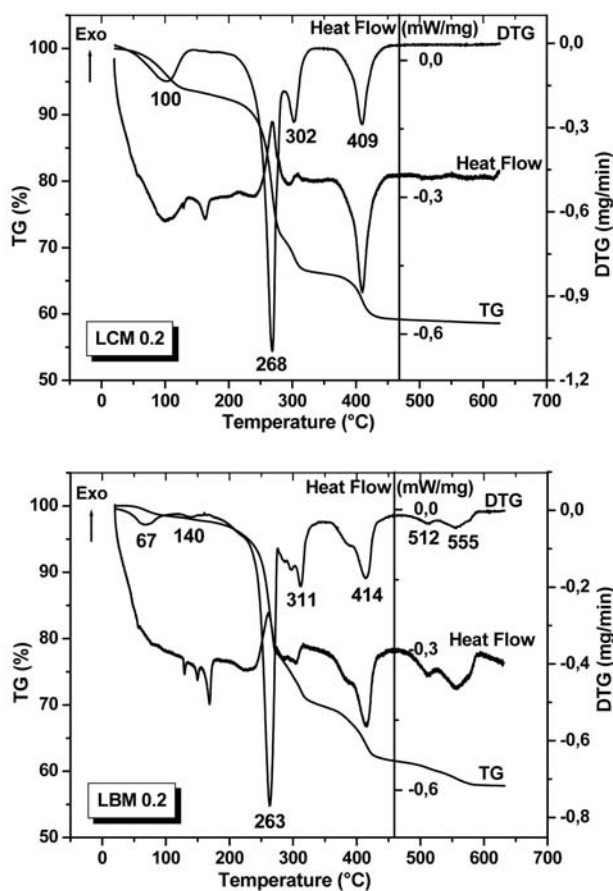


Figure 1. Thermal analyses of the LCM 0.2 and LBM 0.2 samples.

3.2. XRD and SEM Characterization

As mentioned in the previous section, the $\text{La}_2\text{Mo}_2\text{O}_9$ material undergoes a slight structural change at around 580 °C. The compound crystallizes in two forms known as the low temperature α $\text{La}_2\text{Mo}_2\text{O}_9$ monoclinic form (JCPDS file 28-0509) and the high temperature β $\text{La}_2\text{Mo}_2\text{O}_9$ cubic form, whose space group is P_{213} .^{3,4,20} However, the α form could be considered as a slight modification of the cubic β form, because the change in α form is quite small and marked by the presence of low intensities and the splitting of some X-ray reflection lines.^{4,20}

Figure 2 shows the powder X-ray diffraction patterns for undoped $\text{La}_2\text{Mo}_2\text{O}_9$ material, obtained by annealing for 6 hours at different temperatures. It may be noted that at low temperature (200 °C) the material is almost amorphous. From 400 °C, the diffraction peaks emerge and become progressively intense, particularly at 800 °C indicating that the material has become well crystalline.

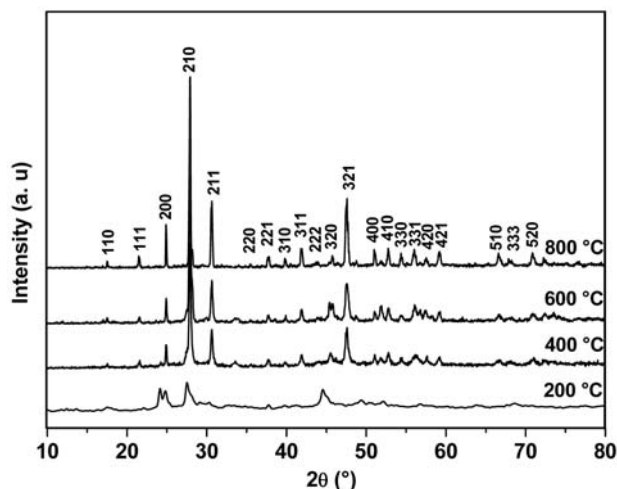


Figure 2. Powder X-ray diffraction pattern of undoped $\text{La}_2\text{Mo}_2\text{O}_9$ at different annealing temperatures.

The reflection from the (200) plane was used for the determination of the average crystallite size T , from the Debye-Scherrer formula (equation 2):²¹

$$T = \frac{C\lambda}{B \cos \theta} = \frac{C\lambda}{(B_M^2 - B_S^2)^{\frac{1}{2}} \cos \theta} \quad (2)$$

where λ is the wavelength of the X-rays (T and λ have the same units), θ the diffraction angle, C is the Scherrer crystal shape factor, generally close to unity (~ 0.9), and B is the full-width at half-maximum (FWHM) of the peak (radians), corrected for instrumental broadening, B_M of the (200) reflexion (in the LCM and LBM samples) and B_S is the FWHM of the (200) reflexion in a standard sample of $\alpha\text{-La}_2\text{Mo}_2\text{O}_9$. A highly crystalline sample with a diffraction peak in a similar position to the one of the standard sample is chosen and this gives the measure of the broadening due to instrumental effects. Thus, the average crystallite size value of the highly crystalline $\alpha\text{-La}_2\text{Mo}_2\text{O}_9$ annealed at 800 °C is estimated to be ~ 50 nm. Cell parameters were calculated by cell parameters refinement program (CELREF V3),²² and the lattice parameter calculated for undoped $\text{La}_2\text{Mo}_2\text{O}_9$ is $a = 0.7157$ nm, which is in good agreement with the literature values.^{4,20,23} Other studies have discussed the relationship between the crystalline structure of both α and $\beta\text{-La}_2\text{Mo}_2\text{O}_9$ forms and their transport properties.^{4,20,24}

Figures 3 shows the X-ray diffraction (XRD) patterns of the LCM and LBM materials calcined at 800 °C

for different amounts of Ca and Ba doping between 0.05 and 0.2 respectively.

For Ca doping, the peaks are sharp, intense and identical to those of the undoped $\text{La}_2\text{Mo}_2\text{O}_9$, except for the appearance of small peaks at high doping content, corresponding to 2θ equal to 28.3°, 46.4° and 48.6°. These peaks can be attributed to the presence of CaMoO_4 secondary phase which is observed at high doping content by X. P. Wang et al.⁶, Subasri et al.⁷ and D. Marrero-Lopez et al.⁹ It can also be explained by a supersaturation of the solid solution. For Ba doping, the peaks are well resolved and recorded at the same positions as those of the undoped $\text{La}_2\text{Mo}_2\text{O}_9$. Two new small peaks are observed at high content of doping agent for $2\theta = 26.56^\circ$ and 32.12° ; characterizing the presence of the BaMoO_4 secondary phase. The two CaMoO_4 and BaMoO_4 secondary phases that appear in the LCM and LBM systems, respectively, are concomitant ones to the $\beta\text{-LCM}$ and LBM forms. They indicate the solubility limit or the limited diffusion

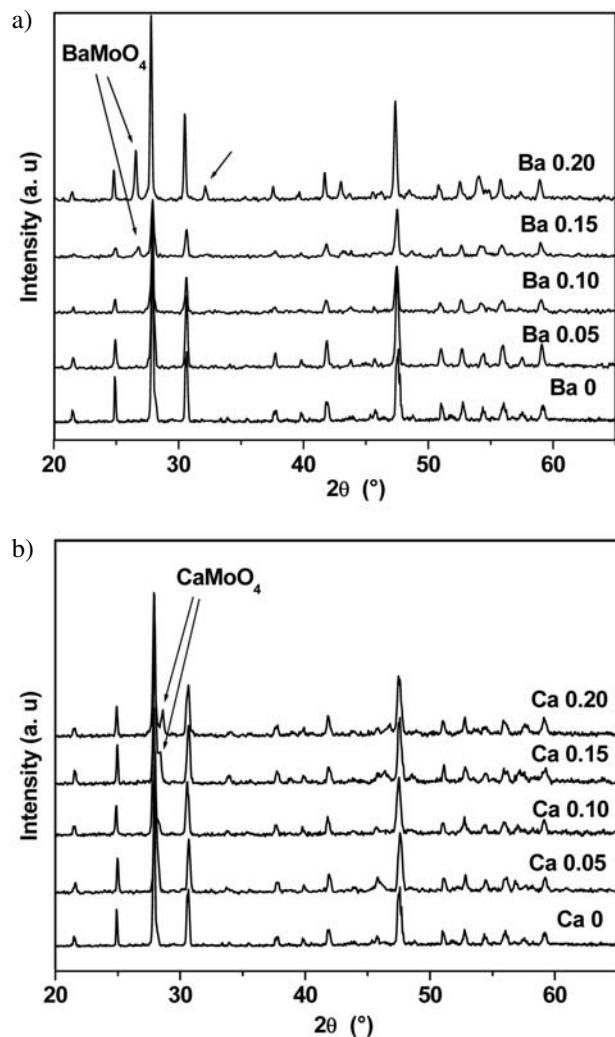


Figure 3. X-ray diffraction diagrams of LCM (a) and LBM (b) systems calcined at 800 °C for 6 hours.

of the dopant in the crystal lattice. They were observed previously by Subasri et al.⁷, He et al.⁸, and Marrero-Lopez et al.⁹

A plot of the lattice parameters of the LCM and LBM materials versus Ca and Ba contents respectively is shown in Figure 4. It may be used to estimate the solubility limits of Ca and Ba in the undoped phase respectively. For Ca doping, the curve decreases firstly to a minimum value of $x = 0.05$ corresponding to $a = 0.7148$ nm, then increases to a maximum at around $x = 0.10$, which corresponds to $a = 0.7158$ nm, and decreases again with doping agent content. The variation in lattice parameter is explained by the size difference between the Ca^{2+} and La^{3+} cations. Indeed, the substitution of a portion of La^{3+} cations by Ca^{2+} which is smaller (ionic radius of $\text{Ca}^{2+} = 0.118$ nm and $\text{La}^{3+} = 0.1216$ nm)²⁵ causes the formation of O^{2-} vacancies and leads to the shrinkage of the lattice at first ($x \leq 0.05$), and to its expansion in the second case ($0.05 < x \leq 0.10$).⁶ In the last step ($x > 0.10$), the curve decrease can be attributed to the relative contents of oxygen vacancy ($\text{Vo}^{\bullet\bullet}$) and localized defect associations (e.g. $\{\text{Ca}'_{\text{La}} \text{Vo}^{\bullet\bullet}\}$ and $\{\text{La}'_{\text{La}} \text{Vo}^{\bullet\bullet}\}$) have changed with the increasing Ca doping. That is, the defect associations began to form when the dopant content reached a certain dopant content x , while the oxygen vacancy is believed to produce a larger lattice contraction than defect associations.⁸

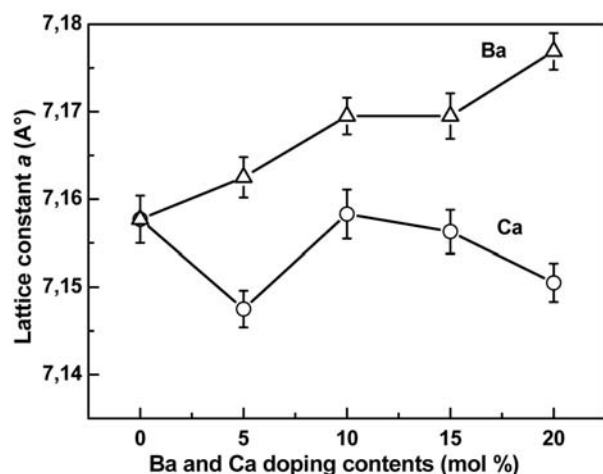


Figure 4. The variation of the lattice constant of the LCM and LBM materials with Ca and Ba doping content.

For doping by Ba^{2+} cation, we can notice a different behavior (Figure 4). The lattice parameter values are larger and increase firstly, between $x = 0$ and $x = 0.10$, with the amount of Ba^{2+} , stabilizing between $x = 0.10$ and $x = 0.15$ and after that, the lattice parameter increases again. This behavior is explained by the fact that replacing the lanthanum La^{3+} cations by the more voluminous Ba^{2+} ones (ionic radius 0.147 nm) leads to the expansion of the lattice and therefore the cell volume increases.^{8,9} We note that we have not obtained the same shape of lattice parameter plot as in the case of the samples prepared by the sol-

id method.^{8,10} However, our plot is similar to the one obtained by D. Marrero-López et al.,⁹ which confirms that the variation of the lattice parameter with x content depends on the preparation method.

From the lattice parameter plots of Figure 4 we can say that the solubility limit is about $x = 0.1$ for the two dopants. This is confirmed by the appearance of small peaks characterizing the secondary phases in the diffractogrammes (Figure 3). This is close to the value found by He et al.⁸ ($x = 0.08$) using the conventional solid-state method. When using the freeze-drying method, Lopez et al.⁹ have found a value of $x = 0.05$ for calcium and $x = 0.075$ for barium. A value of $x = 0.04$ of calcium was also found by Subasri et al.,⁷ using the wet chemical procedure, but up to $x = 0.1$ of barium, no secondary phase was detected.

The calculated average crystallite sizes of both calcium and barium substituted $\text{La}_2\text{Mo}_2\text{O}_9$ powders, after annealing at 800 °C, were around 35 and 45 nm respectively. This nanostructure cannot be evidenced from the SEM images (Figure 5), probably due to the agglomeration of particles at high temperatures.

Figure 5 shows the SEM images of the LCM and LBM powders calcined at 800 °C, and taken without pressing. In the case of calcium doping, the powder grains accumulate to give a sponge-like morphology; but for Ba doping, the grains are arranged one beside the other to produce the shape of sheets. One can also note that the macro-grain size of the Ba doped materials is slightly larger than the one obtained by calcium doping.

3. 3. Characterization by X-ray Photoelectron Spectroscopy (XPS)

For the XPS analysis, we recorded only the most intense peaks corresponding to the highest photoionization cross-section. For example, we studied the Mo 3d as it has a higher photo ionization cross-section value than Mo 3p. The peaks of La 3d, Mo 3d, O 1s and C 1s, as well as the peaks of the doping agents Ca 2p and Ba 3d have been recorded. These peaks appear quite nicely in the spectra for the LCM and LBM systems by reference to Fermi level (Figure 6). The peaks that characterize the barium are clearer than those of calcium, despite the use of similar quantities of both dopants. This is due to the larger value of the photoionization cross-section of the Ba 3d core level, by comparison to the Ca 2p core level.

3. 3. 1. Materials Composition at the Surface

The calculated surface atomic compositions of LCM and LBM materials calcined at 800 °C for six hours, expressed in atomic percent (at. %), are summarized in Table 1. For both systems, we note that the molybdenum content is slightly higher than the lanthanum one. This may be due, firstly, to the substitution of a portion of the lanthanum atoms by doping Ca or Ba elements, secondly,

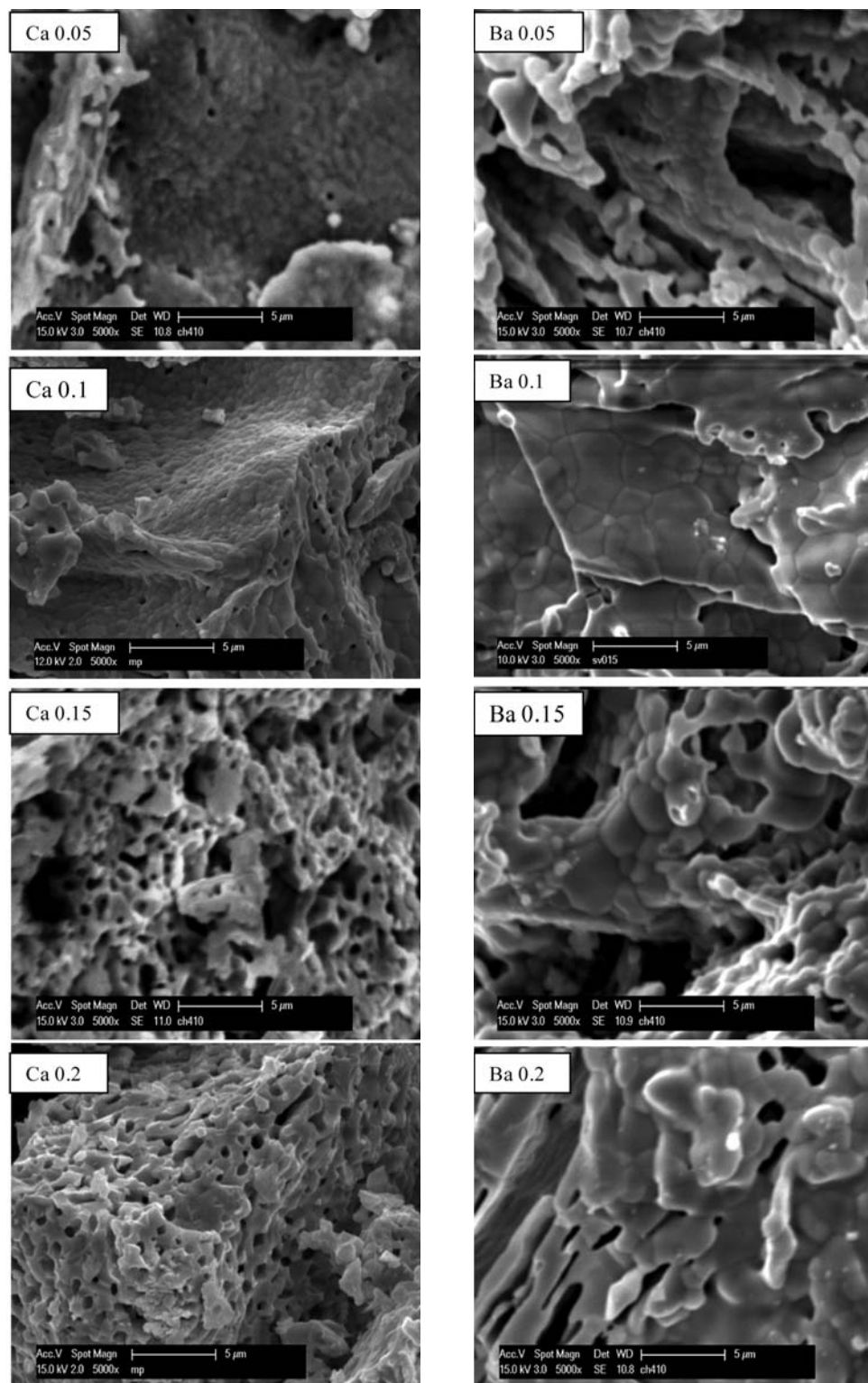


Figure 5. SEM images of LCM and LBM powders calcined at 800 °C doped with Ca and Ba

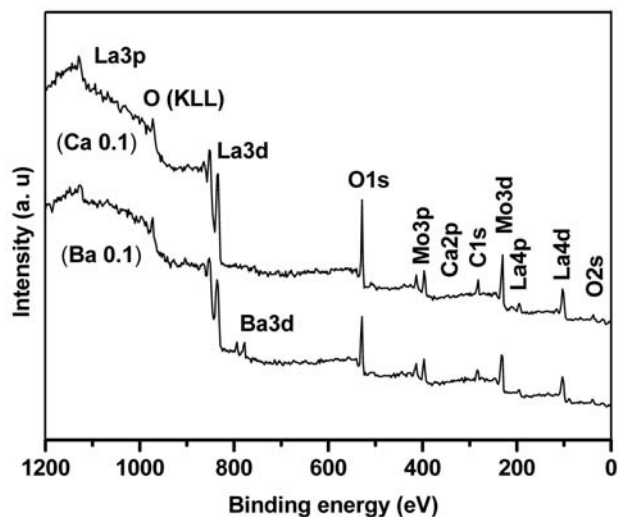
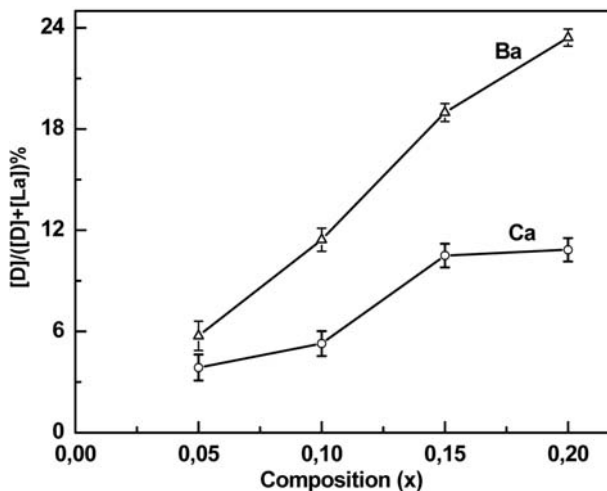
the lanthanum atoms are engaged with oxygen in polyhedra with a larger structure than those made by the molybdenum.^{4,24} In this structure, the oxygen ions that surround each lanthanum atom are more numerous than those which surround the molybdenum atom. In our opinion,

this may allow the molybdenum atoms to move towards the surface more easily than the lanthanum atoms.

Table 1 also shows that the amount of barium at the surface is relatively greater than that of calcium, in particular at high doping content.

Table 1. The surface atomic composition ($\pm 0.1\%$) of LCM and LBM systems

Composition (x)	%La		%Mo		%O		%C		%Ca	%Ba
	LCM	LBM	LCM	LBM	LCM	LBM	LCM	LBM	LCM	LBM
0.05	11.5	9.4	12.9	10.5	51.5	49.8	23.6	29.5	0.46	0.57
0.10	11.7	9.8	13.3	12.4	49.8	50.3	24.5	26.2	0.65	1.27
0.15	10.1	9.4	10.4	13.1	48.0	50.3	29.1	24.9	1.18	2.21
0.20	10.1	8.1	10.7	10.2	52.1	50.7	25.7	28.3	1.23	2.49

**Figure 6.** XPS spectra of LCM 0.1 and LBM 0.1 powders calcined at 800 °C.**Figure 7.** Percentage change of Ca and Ba (D) doping agents at the surface: measured XPS values versus nominal composition.**Table 2.** Surface atomic ratios of LCM and LBM materials.

Composition (x)	O/La*		O/Mo*		La/Mo*		D/(D+La)**	
	LCM	LBM	LCM	LBM	LCM	LBM	LCM	LBM
0.05	4.46	5.28	3.98	4.71	0.89	0.89	3.86 \pm 0.77	5.74 \pm 87
0.10	4.25	5.12	3.74	4.05	0.87	0.79	5.28 \pm 0.74	11.44 \pm 0.69
0.15	4.73	5.33	4.58	3.84	0.96	0.72	10.50 \pm 0.70	18.98 \pm 0.54
0.20	5.12	6.23	4.83	4.94	0.94	0.79	10.84 \pm 0.69	23.42 \pm 0.50

* $\pm 0.03\%$ ** D = Ca for LCM and Ba for LBM materials

Selected surface atomic ratios measured for the LCM and LBM materials are summarized in Table 2. It is found that, the La/Mo ratios in the case of calcium doping are close to the unity, but are much smaller for the barium doping. Similar values have been observed by Gunasekaran et al. during the study of $\text{La}_{1-x}\text{Ba}_x\text{MnO}_3$ mixed oxide.²⁶ These authors found that the lanthanum atomic concentration remarkably decreases when barium quantities varied from 5 to 20 %.

It is also noteworthy that the calcium atomic content values measured at the materials surface are smaller than expected from the used synthesis ingredients, but for the barium the stoichiometry is more respected. The variation of these percentages is also plotted in Figure 7. For calci-

um, there is saturation above $x = 0.15$ at the surface which is greater than the limit of solubility in the bulk of material ($x = 0.10$) given by XRD data. However, for Ba, this variation was practically linear, with no saturation above $x = 0.15$ at the surface.

3.3.2. C1s Core Level Analysis

A typical example of carbon C 1s spectra obtained for all samples is shown in the Figure 8.

A straightforward curve fit of the C 1s peak retrieves three components. The most intense peak having 284.6 eV as the binding energy is attributed to carbon of natural contamination often found in XPS analysis.¹⁸ The peaks

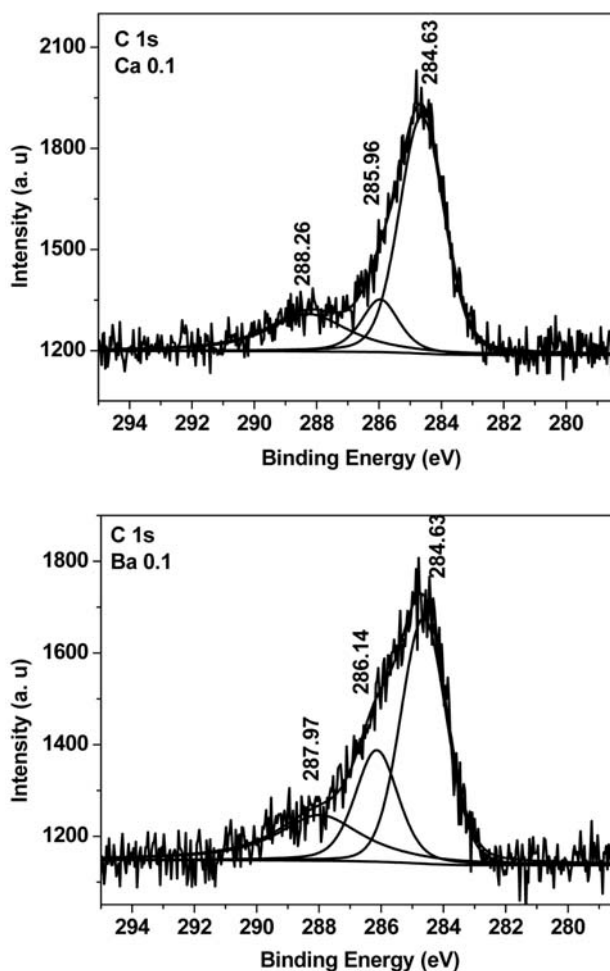


Figure 8. XPS C 1s region of LCM 0.1 (Ca 0.1) and LBM 0.1 (Ba 0.1) samples.

located at about 286 and 288 eV are probably due to the hydrocarbon organic molecules and CO_2 molecules adsorbed on the surface, respectively.²⁷ It is very relevant to note the complete absence of peaks at ~ 282 eV, ~ 290 eV and 291.4 eV. The first observation excludes the formation of metal carbides.²⁸ The second one excludes the formation of calcium carbonate CaCO_3 and barium carbonate BaCO_3 , while the third one, excludes the formation of lanthanum carbonate $\text{La}_2(\text{CO}_3)_3$ at the surface of the LCM and LBM materials.^{28,29} As a consequence, we can conclude that, the observed carbon contamination results from a physical adsorption, without modification of the surface properties of the LCM and LBM materials.

3. 3. 3. Binding Energy Analysis

Purely for reasons of comparison, the bibliographic data of simple oxides and mixed oxides described in this work are summarized in Table 3. A slight difference is observed between the values of the binding energies of elements in simple oxides and those of mixed oxides. The measured binding energies of La $3d_{5/2}$, Mo $3d_{5/2}$, Ba $3d_{5/2}$, Ca $2p_{3/2}$ and O 1s core-levels of LCM and LBM materials are compiled in Table 4. These binding energies are independent of doping levels.

A typical set of XPS spectra recorded for the LCM and LBM samples sintered at 800 °C are shown in Figure 9. For the Ba and Ca spectral regions, we notice, as expected, an improvement in their shapes with increasing dopant content as shown by Figures 9a and 9b.

All La $3d$ spectra show a spin-orbit splitting (La $3d_{5/2}$ and La $3d_{3/2}$) varying between 16.5 and 16.9 eV for the LCM, and 16.7 and 17.0 eV for the LBM systems

Table 3. Binding energy of the elements La, Mo, Ba, Ca and O (eV) of some oxides

Compound	Element					Reference
	La $3d_{5/2}$	Mo $3d_{5/2}$	Ba $3d_{5/2}$	Ca $2p_{3/2}$	O 1s	
La_2O_3	834.9				530.8	This work
La_2O_3	834.8				530.1	34
MoO_3		232.4			530.5	This work
$\text{La}_2\text{Mo}_2\text{O}_9$	834.6	232.4			530.8	This work
Mo^{6+}		232.2			39	
Mo^{5+}		230.8				
Mo^{4+}		229.3				
Mo^{3+}		228.3				
Mo^0		227.6				
CaO				346.5	530.8	This work
CaO				~ 346.5		28 (page 69)
BaO			~ 779.1			28 (page 139)
$\text{La}_{1.8}\text{Dy}_{0.2}\text{Mo}_2\text{O}_9$ (Mo^{6+})	834.7	232.1			530.4	13
(Mo^{5+})		231.7			532.4	
(Mo^{4+})		229.1				
(Mo^0)		227.7				
BaMoO4			~ 779.5			28 (page 139)
CaMoO4				~ 347.2		28 (page 69)
Hydroxides					~ 531.5	28 (page 45)

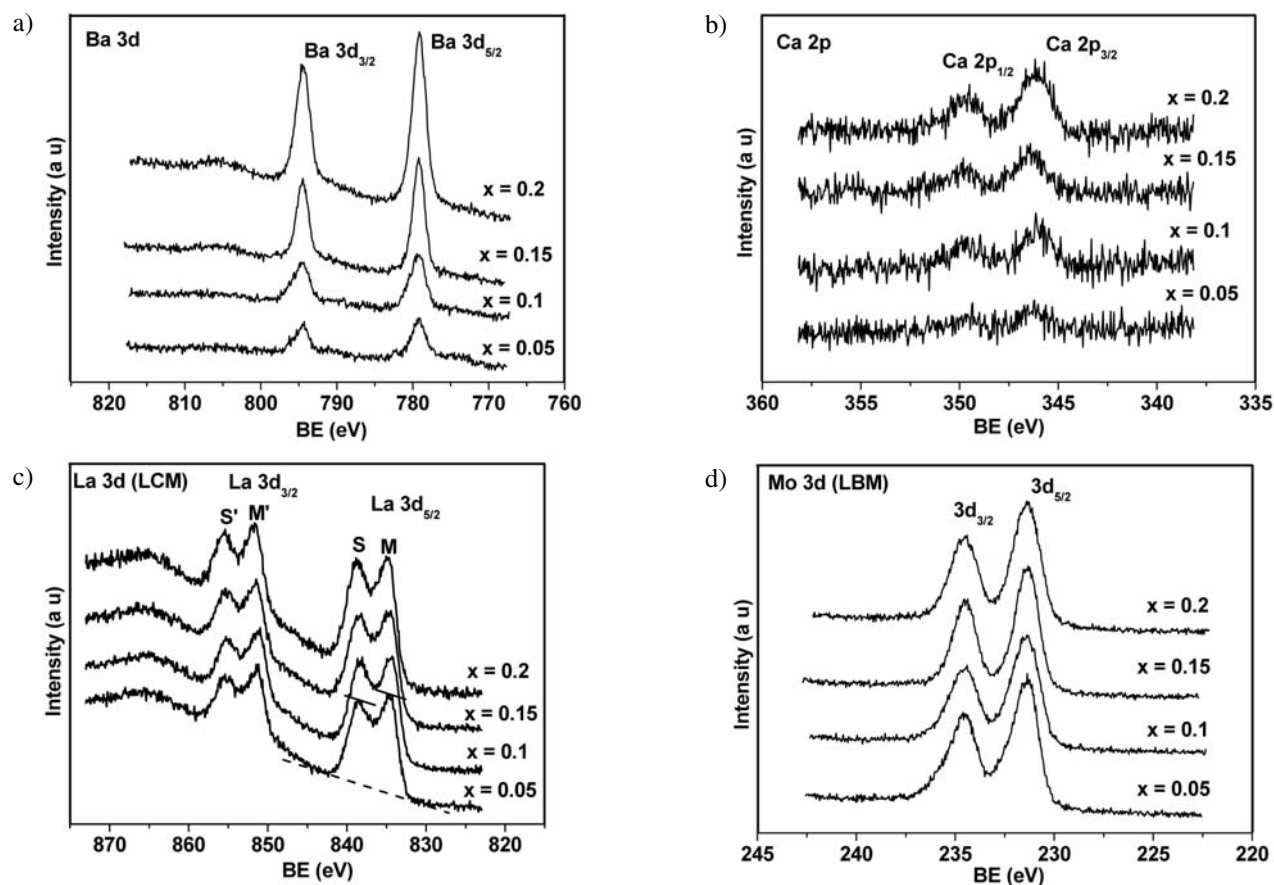


Figure 9. Typical examples of XPS lines for (a) Ba 3d, (b) Ca 2p, (c) La 3d in LCM and (d) Mo 3d in LBM powders at 800 °C respectively. For (c), dotted line indicates the assumed background intensities and continuous line is guide for the eyes.

(Table 4). Both La 3d_{5/2} and 3d_{3/2} peaks exhibit clear doublet structures due to multiplet splitting (Figure 9c). These results from two different screening processes of the initially empty 4f orbital, resulting from the creation of the 3d core hole, after the photoelectron emission process.^{30,31} For the unscreened or “poorly screened” state (M and M’ peaks on Fig. 9c), the 4f empty level is predominantly screened by electrons belonging to the outermost shell of the La atom, while for the so-called “screened state” (S and S’ peaks in Fig. 9c) electrons belonging to the ligand atom (O 2p in this case) are transferred to the 4f subshell to screen the 3d hole. The two unscreened M and M’ peaks thus correspond to the 3d⁹ 4f⁰ final state, and the screened S and S’ peaks correspond to the 3d⁹ 4f¹L final

state, where L stands for one O 2p hole. The degree of overlapping between these two states is very large, because the energy difference is small (~ 4 eV). This result comes from the fact that the energy difference between the La 4f and O 2p levels is comparable to the Coulomb energy between the La 3d core hole and 4f electron.³⁰ By comparison, all spectra of the La 3d region of the LBM and LCM systems are identical to those of the La₂O₃ and La₂Mo₂O₉ compounds and the binding energy of the La 3d_{5/2} peaks reported in Table 4, are also very close to the values of the 3d_{5/2} binding energy of materials whose lanthanum oxidation state is +3.

The energy gap ΔE_j (3d_{3/2}–3d_{5/2}) values of the spin-orbit splitting in the La 3d regions for the Ca and Ba

Table 4. Binding energies (eV) of the La 3d_{5/2}, Mo 3d_{5/2}, Ba 3d_{5/2}, Ca 2p_{3/2} and O 1s core-levels for the LCM and LBM materials calcined at 800 °C

Composition (x)	La 3d _{5/2}		Mo 3d _{5/2}		O 1s		Ca 2p _{3/2}	Ba 3d _{5/2}
	LCM	LBM	LCM	LBM	LCM	LBM	LCM	LBM
0.05	834.6	834.6	232.3	232.1	530.3	530.2	347.4	779.9
0.1	834.6	834.8	232.3	232.1	530.3	530.3	347.3	780.1
0.15	834.8	834.7	232.3	232.2	530.5	530.2	347.0	779.9
0.2	834.7	834.7	232.2	232.1	530.5	530.2	347.3	780.0

doped systems are grouped in Table 5. These values show a slight difference compared with La 3d of lanthanum alloy ($\Delta E_j = 16.78$ eV)²⁸ and with those of La₂O₃ and La₂Mo₂O₉ reference compounds ($\Delta E_j = 17.0$ eV). The same data presented in Figure 10 are clearly showing that, for Ba doping, giving consistently larger ΔE_j values which initially decrease and then increase, but for Ca doping, the ΔE_j gradually decreases.

Table 5. ΔE_j values (± 0.1 eV) and satellite (S) to main (M) peak intensity ratio of the La 3d core levels for the LCM and LBM systems as a function of doping.

Compo- sition (x)	LCM		LBM	
	ΔE_j (eV)	I_S/I_M (3d _{5/2})	ΔE_j (eV)	I_S/I_M (3d _{5/2})
0.05	16.9	0.85	17.0	0.84
0.10	16.7	0.86	16.7	0.83
0.15	16.6	0.86	16.8	0.82
0.20	16.5	0.86	17.0	0.84

Theoretically, the energy difference between the doublet components, ΔE_j , is dependent on the spin-orbit constant, ξ_{nl} , which is related to the expectation value $\langle 1/r^3 \rangle$ of the average radius of the involved orbital. Therefore, this constant increases with the atomic number Z for a given subshell (n and l) and decreases as l increases for a given n .³² It is thus understandable that the energy difference of La 3d components increases when the nuclear effective charge increases. This can occur when the valence electrons move farther away from the nucleus and the core level electrons get closer to the nucleus, causing stronger spin-orbit interaction. As a conclusion, we can say that when the Ca content increases, the observed ΔE_j decreases meaning that the effective La nuclear charge decreases, while the La nuclear charge becomes larger for Ba doping (compared to Ca doping).

The theory also predicts that the satellite to main peak intensity ratio I_S/I_M in the La 3d spectrum and the covalency character of the chemical bonding between the oxygen ligand and the central ion, are proportional to the charge transfer from the O 2p to the metal 4f level.³³ A more covalent bond should present a more intense satellite peak. When replacing the La³⁺, the dopant atom brings one effective additional negative charge; therefore, for maintaining charge neutrality, the host metal cation tends to 'give' an electron and the host oxygen anion tends to 'take' it. Consequently, the electron cloud is relatively less pushed away from La toward O when the covalent character increases.^{34,35} This probably occurs for the dopants of covalent character, but for those of ionic character, the electron cloud is more pushed away from La to O anions increasing the ionic character.

Figure 10 shows the I_S/I_M plot of the La 3d_{5/2} component depending on the quantities of calcium and barium

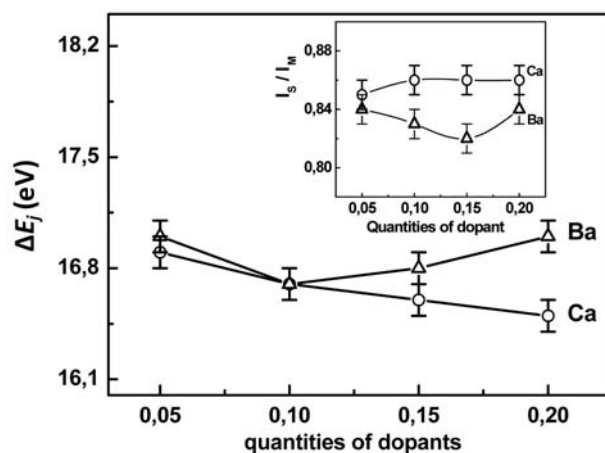


Figure 10. Separation energy (ΔE_j) in the La 3d doublet as a function of Ca and Ba quantities; the inset shows the intensity ratio of the satellite to main (I_S/I_M) peaks in the 3d_{5/2} doublet, versus Ca and Ba doping.

doping agents. It is clear that the ratio is globally greater in the case of doping by calcium, indicating a more intense charge transfer from O 2p to La 4f subshells. Thus, we can say that doping with calcium enhances the covalent character of La–O bonds in a slightly greater manner than doping with barium. Based on the ionic/covalent character classification of oxides, barium oxide has a larger ionic character than calcium oxide.³⁶

The molybdenum Mo 3d region (Figure 9d) presents a doublet structure due to the spin-orbit coupling (Mo 3d_{5/2} and Mo 3d_{3/2}), with the theoretical intensity ratio of 3:2). The binding energy values of the Mo 3d_{5/2} peak (Table 3) are all around 232.3 eV for Ca doping and 232.1 eV for Ba doping, suggesting that molybdenum exists in its highest oxidation state Mo⁶⁺ on the surface of the LCM and LBM systems (see the literature values of Table 2).

Comparatively to the literature results (Tables 2 and 3), it is obvious that Ca and Ba have the oxidation state 2+.

The assignment of the O1s peak components is difficult when several cations of various characters are present in the mixed metal oxide material, which could lead to the formation of several non-equivalent metal-oxygen bonds. For example, a detailed structural study of β -La₂Mo₂O₉ revealed the existence of three types of oxygen anions around the La cations, and three others around the Mo cations with 3 different bond lengths with the metal.²⁴ The surface of these materials being not completely free of impurities (adsorbed carbon oxide and hydroxyl groups for example), this will add another difficulty in the study of the O1s peak. In an oxygen-metal bond, the facility of ejection of an electron from the oxygen O 1s increases with its ionic character. Therefore, the binding energy will be lower.³⁵ As shown above, calcium increases the covalent character and the barium increases the ionic character

Table 6. Positions (eV), full width at half maximum (FWHM) and elemental composition (atomic %) for the different components of the XPS core level O1s lines.

Material & composition	Position (eV)	FWHM	Area (%)	
La ₂ Mo ₂ O ₉	530.20	1.94	64.76	
	531.80	1.95	24.02	
	533.00	1.94	11.20	
(La _{1-x} Ca _x) ₂ Mo ₂ O _{9-δ}	0.05	530.30	1.94	73.17
		531.70	1.78	18.38
		532.90	2.16	8.44
	0.10	530.30	1.94	83.55
		531.60	1.84	11.55
		532.90	1.60	4.89
	0.15	530.30	1.98	74.01
		531.60	2.00	21.83
		533.00	2.33	4.15
0.20	530.30	1.94	75.42	
	531.70	1.60	14.74	
	532.90	2.00	9.82	
(La _{1-x} Ba _x) ₂ Mo ₂ O _{9-δ}	0.05	530.10	1.98	65.99
		531.70	1.87	22.88
		532.90	2.31	11.12
	0.10	530.10	1.95	65.75
		531.70	2.00	32.39
		533.00	2.00	1.86
	0.15	530.20	1.81	74.48
		531.50	2.00	20.51
		533.00	1.97	5.00
	0.20	530.20	1.99	72.68
		531.50	2.00	20.01
		532.80	2.35	7.29

of the La–O bond. Thus, we expect that the binding energy of oxygen of the crystal lattice will be larger in material doped by calcium than for those doped by barium (1st column for each composition in Table 6).

Figure 11 shows the curve fitting of the oxygen O 1s regions for the two LCM and LBM systems for $x = 0.05$. According to the literature, the peak of higher binding en-

ergy (532.7–533 eV) can be assigned to the oxygen of organic contamination³⁷, the one at 531.5–531.7 eV is due to adsorbed water and carbon dioxide^{37,38}, while the most intense component (binding energy at 530.3 eV for the material doped with calcium and at 530.1–530.2 eV for the material doped with barium) can be undoubtedly attributed to the oxygen lattice of the LCM and LBM mate-

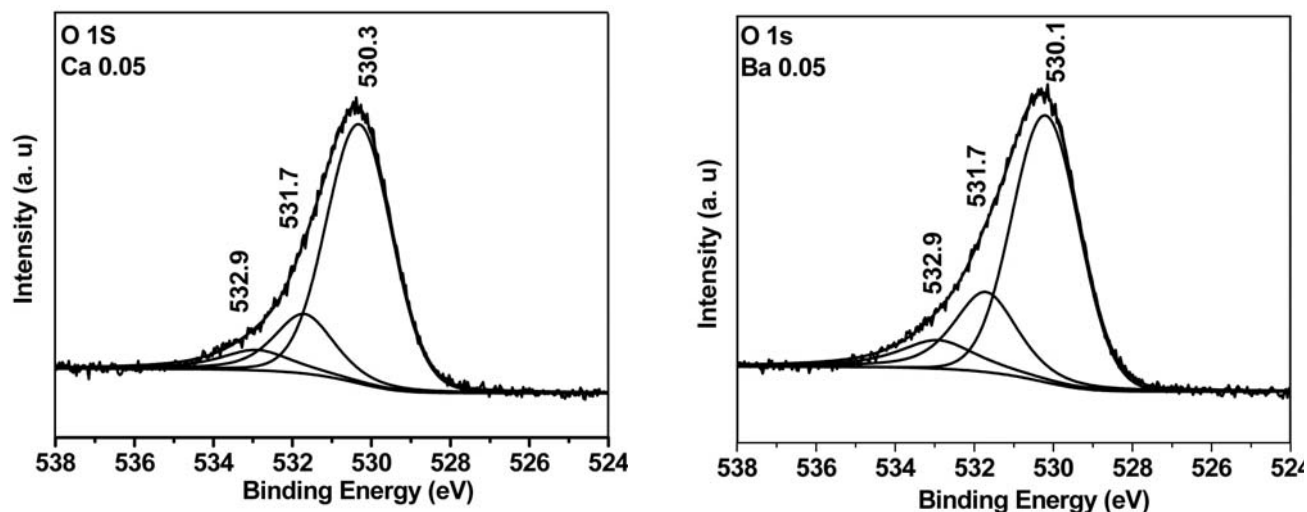


Figure 11. XPS O 1s lines for LCM 0.05 and LBM 0.05 samples.

rials. We can notice that, the oxide O1s peak intensity (about 70 to 75%) is comparable to the sum of the (metal + dopant) intensity, excluding carbon (Table 1). This proves the consistency of our analysis.

In association with Table 6, Table 7 shows that the ratio of the sum of fractions of La, Mo, and dopants (D = Ca or Ba) and that of oxygen is between 0.56 and 0.66 for LCM, and 0.57 and 0.66 for LBM, which means that the three metals make up on average one third of the surface of both materials while the oxygen constitutes two-thirds. Chemically speaking, we can say that the surface has a pronounced anionic character, particularly for LCB system, and lower Lewis acid character, which could refer to possible electrochemical and catalytic properties of interest.

Table 7. Ionic character of the surfaces of LBM and LCM systems.

Composition (x)	([La +Mo +D])/[O]	
	LCM	LBM
0.05	0.66	0.62
0.10	0.62	0.61
0.15	0.61	0.66
0.20	0.56	0.57

4. Conclusion

The $(\text{La}_{1-x}\text{Ca}_x)_2\text{Mo}_2\text{O}_{9-\delta}$ and $(\text{La}_{1-x}\text{Ba}_x)_2\text{Mo}_2\text{O}_{9-\delta}$ materials (x varying from 0.05 to 0.2) prepared by the co-precipitation method have been fully characterized by X-ray diffraction, scanning electron microscopy imaging and x-ray photoelectron spectroscopy technique.

X-rays diffraction showed that the solubility limit of calcium in the material lattice is around 10% ($x \sim 0.1$). At equivalent calcium and barium doping levels, it is found that the barium amount at the surface is larger than that of calcium. The lanthanum and molybdenum cations are in their conventional characteristic oxidation states, 3+ and 6+ respectively. The complete absence of metal carbides and metal carbonates on the surface is a good sign of materials stability in a reducing medium because such solid oxides have been widely used as solid electrolyte solutions in fuel cells to oxidize carbonaceous molecules like methane generating CO, CO₂ and water as combustion products. The examination of XPS La 3d and O 1s peaks shows that the covalent character of La–O bonds enhances with doping by calcium whereas doping by barium increases the ionic character of the bond. The XPS also has showed that oxygen constituted two-thirds of the surface of LCM and LBM materials, which could have interesting electrochemical and catalytic properties. It is also noted that the formation of CaMoO₄ and BaMoO₄ secondary phases has no marked effect on the surface state of the studied materials.

5. Acknowledgements

This work was the result of bilateral scientific collaboration between the University of Jijel (Algeria) and LISE laboratory of the *Research Center on Physics of Matter and Radiation (PMR)*, University of Namur (Belgium). Great acknowledgments are given to the Ministry for higher education and scientific research in Algeria which gave a partial financial support to this work.

6. References

1. W. Kuang, Y. Fan, K. Yao, Y. Chen, *J. Solid State Chem.* **1998**, *140*, 354–360.
2. W. Kuang, Y. Fan, J. Qiu, Y. Chen, *J. Mater. Chem.* **1998**, *8*, 19–20.
3. P. Lacorre, F. Goutenoire, O. Bohnke, R. Retoux, Y. Laligant, *Nature*, **2000**, *404*, 856–858.
4. F. Goutenoire, O. Isnard, R. Retoux, and P. Laccore, *Chem. Mater.* **2000**, *12*, 2575–2580.
5. A. J. Jacobson, *Chem. Mater.* **2010**, *22*, 660–674.
6. X. P. Wang, Q. F. Fang, *Solid State Ionics.* **2002**, *146*, 185–193.
7. R. Subasri, D. Matusch, H. Näfe, F. Aldinger, *J. Eur. Ceram. Soc.* **2004**, *24*, 129–137.
8. T. He, Y. Huang, Q. He, Y. Ji, L. Pei, J. Liu, Z. Lu, *J. Alloys Compd.* **2005**, *388*, 145–152.
9. D. Marrero-López, D. Pérez-Coll, J. C. Ruiz-Morales, J. Canales-Vázquez, M. C. Martín Sedeño, P. Núñez, *Electrochim. Acta.* **2007**, *52*, 5219–5231.
10. B. Yan, M. Li, J. Zhang, K. C. Chou, *Mater. Res. Bull.* **2010**, *45*, 382–387.
11. J. B. Goodenough, Y. H. Huang, *J. Power Source*, **2007**, *173*, 1–10.
12. D. Marrero-Lopez, J. Pena-Martínez, J. C. Ruiz-Morales, D. Pérez-Coll, M. C. Martín Sedeno, P. Nunez, *Solid State Ionics*, **2007**, *178*, 1366–1378.
13. T-Y. Jin, M. V. M. Rao, C-L. Cheng, D-S. Tsai, M-H. Hung, *Solid State Ionics*, **2007**, *178*, 367–374.
14. D. Marrero-Lopez, J. Pena-Martínez, D. Perez-Coll, P. Nunez, *J. Alloys Compd.* **2006**, *422*, 249–257
15. M. Kakihana, *J. Sol-Gel Sci. Techn.* **1996**, *6*, 7–55.
16. Z. G. Yi, Q. F. Fang, X. P. Wang, G. G. Zhang, *Solid State Ionics*, **2003**, *160*, 117–124.
17. Z. Zhuang, X. P. Wang, A. H. Sun, Y. Li, Q. F. Fang, *J. Sol-Gel Sci. Technol.* **2008**, *48*, 315–321.
18. T. L. Barr, S. Seal, K. Wozniak, J. Klinowski, *J. Chem. Soc., Faraday Trans.* **1997**, *93*, 181–186.
19. I. Elliott, C. Doyle and J. D. Andrade, *J. Electron Spectrosc. Relat. Phenom.* **1983**, *28*, 303–316.
20. C. Tealdi, G. Chiodelli, L. Malavasi, G. Flor, *J. Mater. Chem.* **2004**, *14*, 3553–3557.
21. W. Huang, P. Shuk, and M. Greenblatt, *Chem. Mater.* **1997**, *91*, 2240–2245.

22. U. D. Altermatt, I. D. Brown, *Acta Cryst. A*, **1987**, *43*, 125–130.
23. A. Subramania, T. Saradha, S. Mushumathi, *Mater. Res. Bull.* **2008**, *43*, 1153–1159.
24. C. Tealdi, L. Malavasi, C. Ritter, G. Flor, G. Costa, J. Solid State Chem. **2008**, *181*, 603–610.
25. R. D. Shannon, *Acta Crystallogr. Sect. A* **1976**, *32*, 751–767.
26. N. Gunasekaran, S. Rajadurai, J. J. Carberry, N. Bakshi, C. B. Alcock, *Solid State Ionics*, **1995**, *81*, 243–249.
27. T. L. Barr, *J. Vac. Sci. Technol. A*, **1989**, *7*, 1677–1683.
28. J. F. Moulder, W. F. Stickle, P. E. Sobol, K. D. Bomben (Ed.): Handbook of X-ray Photoelectron Spectroscopy, by Perkin-Elmer Corporation, Physical Electronics Division, **1992**, pp 41, 140.
29. P. A. W. Vander Haide, *J. Electron Spectrosc. Relat. Phenom.* **2006**, *151*, 79–91.
30. S. Suga, S. Imada, T. Muro, T. Fukawa, T. Shishidou, Y. Tokura, Y. Moritomo, T. Miyahara, *J. Electron Spectrosc. Relat. Phenom.* **1996**, *78*, 283–286.
31. N. Mannella, A. Rosenhahn, A. Nambu, B. C. Sell, B. S. Mun, S.-H. Yang, S. Marchesini, M. Watanabe, K. Ibrahim, S. B. Ritchey, Y. Tomioka, C. S. Fadley, *J. Electron Spectrosc. Relat. Phenom.* **2006**, *153*, 37–57.
32. D. Briggs, J. T. Grant (Ed.): Surface Analysis by Auger and X-Ray Photoelectron Spectroscopy, IM Publications and Surface Spectra Limited, **2003**, pp. 36.
33. W. Y. Howng, R. J. Thorn, *J. Phys. Chem. Solids*, **1980**, *41*, 75–81.
34. P. Datta, P. Majewski, F. Aldinger, *Mater. Res. Bull.* **2008**, *43*, 1–8.
35. D. A. Pawlak, M. Ito, M. Oku, K. Shimamura, T. Fukuda, *J. Phys. Chem. B*, **2002**, *106*, 504–507.
36. T. L. Barr (Ed.): Modern ESCA, The Principles and Practice of X-ray Photoelectron Spectroscopy, CRC Press: Boca Raton, FL, **1994**, pp 186–187.
37. S. Rousseau, S. Lorient, P. Delichere, A. Boreave, J.P. Deloume, P. Vernoux, *Applied Catalysis B: Environmental*. **2009**, *88*, 438–447
38. D. T. Clark, A. Harrison, *J. Polymer Sci. Polymer Chem. Ed.*, **1981**, *19*, 1945–1955.
39. H. Hixson, P. M. A. Sherwood, *Chem. Mater.* **1996**, *8*, 2643–2653

Povzetek

$(La_{1-x}Ca_x)_2Mo_2O_{9-\delta}$ in $(La_{1-x}Ba_x)_2Mo_2O_{9-\delta}$ ($x = 0,05, 0,1, 0,15, 0,2$) smo pripravili s soobarjanjem pri 800 °C in jih karakterizirali z rentgensko fazno analizo in vrstično elektronsko mikroskopijo. Rentgenski difraktogrami so pokazali prisotnost sekundarnih faz $CaMoO_4$ in $BaMoO_4$ le pri velikih vsebnostih dopantov. Z rentgensko fotoelektronsko spektroskopijo (XPS) smo raziskovali kemijsko sestavo površin dopiranih in nedopiranih materialov ($La_2Mo_2O_9$). Ugotovili smo, da sta valenčni stanji atomov La in Mo 3+ in 6+. Zaradi odsotnosti karbidnih in karbonatnih skupin na površini sklepamo, da ni prišlo do interakcije med ogljikom in kovinskimi atomi, kar omogoča uporabo materialov v kombinaciji z organskimi gorivi; ter da prisotnost sekundarnih faz ni vplivala na kemijsko sestavo površine. Kovalentni značaj vezi La–O je bolj izrazit po dopiranju s kalcijem kot z barijem, kar nakazuje zanimive prevodniške in katalitske lastnosti raziskovanih materialov.